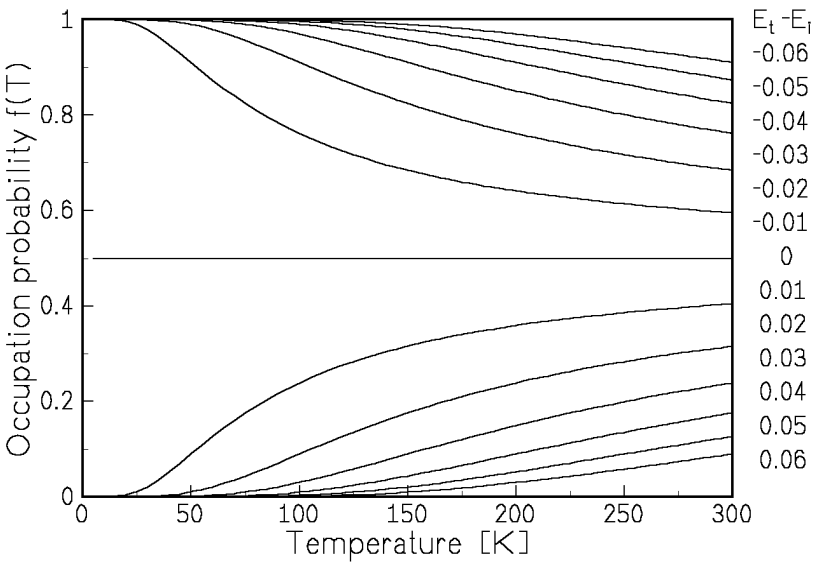

Figure 2.6: Occupation probability of a mid-gap energy level in the SCR calculated from eqs. 2.57 and 2.58, $\sigma_n/\sigma_p = 1$.

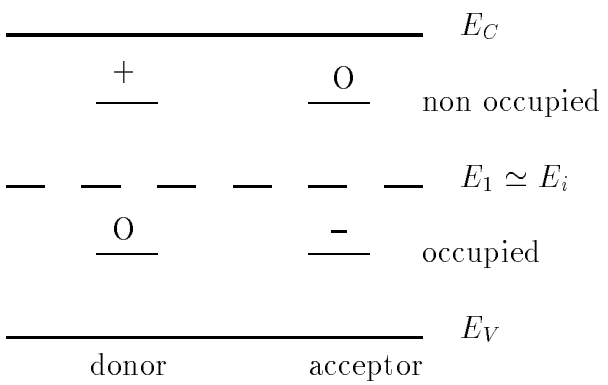

Figure 2.7: Charge state of donors and acceptors in the SCR.

with E_i being the intrinsic Fermi-level and σ_n and σ_p the cross section of the trap for electrons and holes, respectively [19]. In a similar way as E_F in the ENB E_1 allows the description of the occupation probability $f(T)$ in the SCR :

$$f_T(T) = \frac{1}{1 + exp\left(\frac{2(E_T - E_1(T))}{k_B T}\right)}, \tag{2.58}$$

which has been expressed in terms of emission rates already in eq. 2.54.

In fig. 2.6 $f(T)$ is shown for various energy levels close to E_i. As can be seen the occupation probability varies significantly only in the range $E_i \pm$ 0.06 eV. Therefore the energy levels in the SCR are almost empty if $E_T > E_1$ and almost filled if $E_T < E_1$. Donor-like states will be neutral in the lower half of the bandgap, because they are filled, whereas acceptor-like states will be neutral in the upper half and negatively charged in the lower half of the gap (see fig. 2.7). Thus donor-like states contribute to the space charge only when they are in the upper half and acceptor-like states only in the lower half of the energy gap. The contribution of energy levels close to mid-gap is governed by the temperature.

2.5 Detector Operation

Ionising particles passing a silicon detector generate electron-hole pairs along their tracks. The number is in proportion to the particles energy loss. The creation of a single electron-hole pair requires a mean energy of 3.6 eV. Thus the energy loss in the silicon can be measured by "counting" the total number of created pairs. Therefore an electrical field is applied to separate electrons and holes before they recombine. Due to the field the electrons drift to the anode while the holes drift to the cathode. This is termed *charge collection*. The drifting charge carriers influence the signal at the electrodes. The signal is picked up as a current pulse, the integration of which equals the total charge generated in the silicon, and thus is a direct measure of the deposited energy. The process is shown schematically in fig. 2.8. The read-out stage

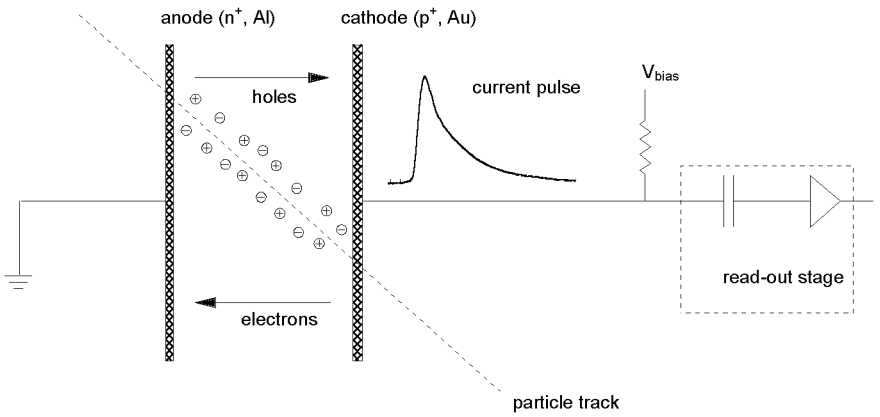

Figure 2.8: A schematic plot of detector operation. In the read-out stage the current pulse is decoupled from the leakage current (dc) and amplified.

conventionally consists of an RC network, a charge-sensitive preamplifier followed by a pulse shaping filter amplifier. [10]

Leakage current and detector capacitance are a source of noise to the system.

[10] A comprehensive overview of detector electronics and pulse processing can be found e.g. in [20].

The noise can be described by the following equation [21]:

$$\sigma^2_{noise} = KI\tau + \frac{LC^2}{\tau} + M, \tag{2.59}$$

where K, L and M are parameters depending on the system, τ is the shaping time constant, and I and C are the current and the total input capacitance, respectively. From eq. 2.59 it becomes obvious that both current and capacitance should be as small as possible. While the capacitance is mainly determined by the detector geometry, the leakage current is governed also by temperature which can be controlled by the experimenter.

In order to ensure correct energy detection it is necessary to completely collect the generated electrons and holes. Hence, a high electrical field extending over the full detector thickness is necessary. [11] This can be achieved by applying a reverse bias voltage to a diode (p^+-n or Schottky) higher than the depletion voltage. For $V = V_{fd}(x_n = d)$ the electrical field across the detector thickness follows from eq. 2.16 :

$$\mathcal{E}_{fd}(x) = \frac{qN_{eff}(x-d)}{\epsilon_S}. \tag{2.60}$$

Replacing N_{eff} by the right side of eq. 2.26 one gets

$$\mathcal{E}_{fd}(x) = \frac{2V_{fd}}{d}(1 - \frac{x}{d}). \tag{2.61}$$

Then the overbias simply increases the field in proportion to $V - V_{fd}$:

$$\mathcal{E}(x) = \mathcal{E}_{fd}(x) + \frac{V - V_{fd}}{d}. \tag{2.62}$$

The limits of the overbias are given by the depletion voltage and the breakdown voltage. The lower limit, which is the depletion voltage, can be kept small by using thin detectors with a low effective doping concentration (see eq. 2.25). Hence, silicon detectors are usually 250 to 3000 μm thick and made of high resistivity material. The breakdown voltage, which is mainly determined by the technology (see sec. 2.2), sets an upper limit, because the current and thus also the noise at voltages above breakdown increases very rapidly.

2.6 Manufacture of Detectors

As explained in the preceding section silicon detectors are made out of high resistivity n-type material ($\rho > 2$ kΩcm). Wafers of some 100 μm thickness are cut from an ingot with a diameter of 3 or 4 inch .

In 1980, Kemmer introduced the *planar technology* to fabricate silicon detectors from the naked wafer [22, 23]. This method, which is now in common usage, is described briefly in the following. The first step is the *oxidation* of the polished wafer. The main effect of the oxidation is the elimination of the surface leakage

[11] A further reason to apply high fields is the requirement of a short charge collection time, see sec. 2.7.

current, and therefore it is also called *passivation*. The oxide layer also protects the wafer during fabrication and later the detector itself. The oxidation process is a chemical reaction between silicon and oxygen, which takes place at high temperature ($\approx 1000°C$) and lasts several hours. Oxides may be grown dry ($Si + 2O \rightarrow SiO_2$) or wet ($Si + 2H_2O \rightarrow SiO_2 + 2H_2$). Also additives such as HCl (hydrochloric acid) or TCE (trichlorethylene) may be used to change the properties of the oxide. Because the precise parameters govern rather sensitively the quality of the oxide they are often closely guarded secrets of the manufacturer. While the oxidation process is of little concern for the bulk material (see also sec. 7.1.2) it has strong influence on the radiation hardness of the detector surfaces (see e.g. [24, 25]).

To realise the required detector geometry selected areas of the oxide have to be removed. This is usually achieved by photolithography and successive etching. First a mask has to be prepared with a pattern of the designed geometry. After the wafer is coated with photo-resist, the pattern is transferred by shining UV-light through the mask onto the wafer. During the following development, the exposed areas of photo-resist will remain or be washed away, depending of the kind of photo-resist in use. Then those parts of the oxide which are not covered by the photo-resist are removed by etching. The opened windows are then ready e.g. for ion implantation or evaporation of gold. In case of complicated structures the procedure described above must be be carried out repeatedly.

For the fabrication of Schottky diodes as used in this work the next steps are the evaporation of gold on the front side to build the Schottky contact, and aluminium

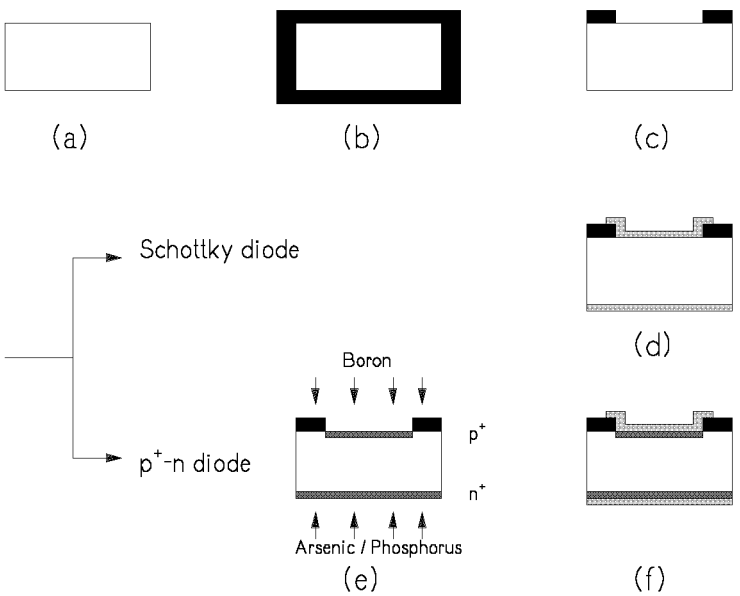

Figure 2.9: Fabrication process : (a) n - Si wafer, (b) oxide passivation, (c) opening of windows, (d) evaporation of gold and aluminium for Schottky diodes, (e) ion implantation, (f) evaporation of aluminium.

on the rear side to form an ohmic contact [16].

The p^+ layer of the p^+-n junctions is realised using the method of *ion implantation*. Compared to the diffusion process this technique is advantageous, because a lower processing temperature is required, and a very precise tailoring of the doping profile is possible. In many cases the rear side of the wafer has a n^+ layer to improve the contact, which is made by implanting e.g. phosphorus or arsenic, while boron is used for the front side. To have good ohmic contacts aluminium is deposited additionally by evaporation on both sides.

Finally the wafer has to be cut very carefully to avoid rough edges, which could be a source of leakage current. The process steps are summarised schematically in fig. 2.9.

2.7 Radiation Environment of the SCT

In the remainder of this chapter the ATLAS inner detector is described as an example for the high radiation level expected in future experiments of particle physics. The description of the ATLAS inner detector and the semiconductor tracker (SCT) follows mainly the technical proposals [26, 27].

The basic functions of the ATLAS inner detector are :

- precision transverse momentum (p_T) measurements of leptons;
- electron and photon identification at high luminosity;
- τ and b tagging at lower luminosity running.

In order to achieve an optimum solution for the imposed requirements a combination of three technologies has been chosen : The end-cap part and the outer barrel consist of transition radiation detectors, in the forward region microstrip gas counters (MSGC) will be used and a SCT is placed in the centre of the inner detector. The SCT consists of the barrel silicon, the forward gallium arsenide (GaAs), the barrel and forward pixels, and the vertexing layer. The over-all length of the inner detector is about 7 m and the radius is 115 cm. Six precision layers of silicon pixel and microstrips are foreseen in the barrel region which are approximately evenly spaced between the minimum and maximum radii of 10 and 60 cm. Two pixel layers at radii of 11.5 and 16.6 cm and four equally spaced silicon strip layers at radii from 30 cm to 60 cm together with the transition radiation tracker (TRT) in the outer region will provide the required p_T resolution. Besides the concept outlined above also a design for the forward region based on silicon is under consideration (see fig. 2.10). The barrel silicon layers can be found parallel to the z-axis. Perpendicular to the z-axis and covering the forward direction silicon disks are planned instead of the MSGCs. At about z = 1.5 m and R < 30 cm three GaAs disks are foreseen.

The radiation the detector system has to withstand has two main sources, particle production at the interaction point and albedo neutrons emitted from the calorimeter which surrounds the inner detector back into the central tracking region.

The albedo neutrons arise from hadron initiated nuclear reactions within the calorimeter absorber material. Typical energies are in the MeV range. The inner detector is shielded by a polythene absorber which reduces the flux of albedo neutrons by a factor of 10.

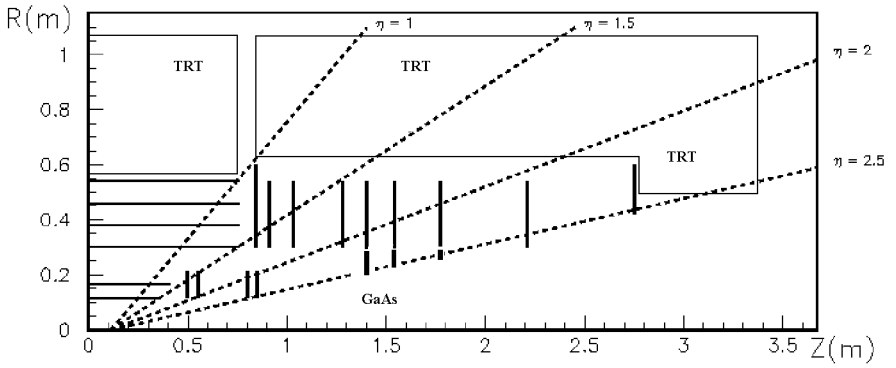

Figure 2.10: Modified tracker layout for the inner detector [26]. Except the TRT and the three GaAs wheels at about Z = 1.5 m all detector components are based on silicon.

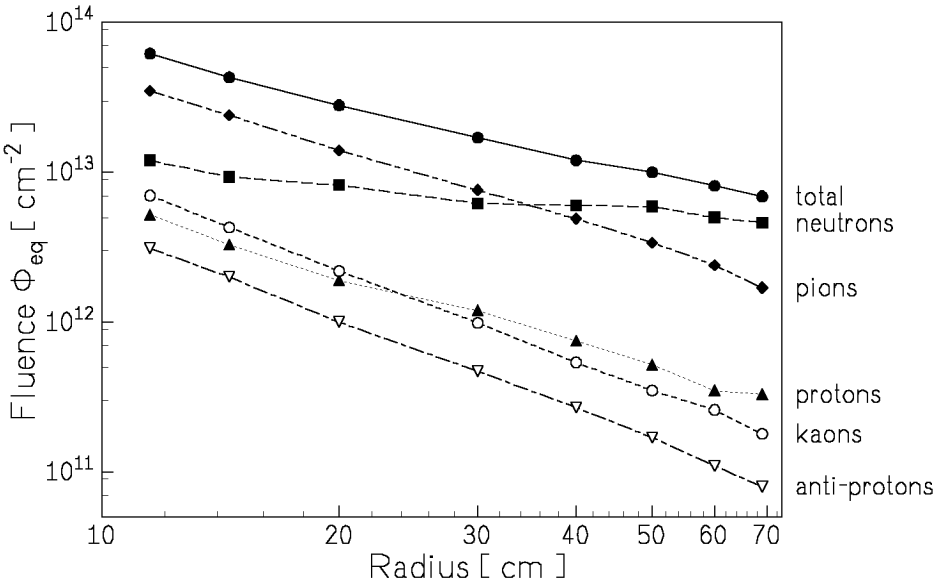

Figure 2.11: Expected particle fluences per year equivalent to 1 MeV neutrons versus radius in the SCT. Note that the pion fluence is dominating for radii smaller 35 cm, for greater radii neutron fluence dominates. Flux calculation by G. Gorfine [28].

However, the particle fluxes created in the primary p-p collisions and from secondaries directly associated with these particles will dominate the radiation field. In order to obtain reliable estimates on the particle fluxes and distributions comprehensive Monte Carlo simulations have been performed by Gorfine and Taylor [29], and recently updated [28]. The 1 MeV neutron equivalent fluxes (cm^{-2} y^{-1}) of several particels are shown in fig. 2.11. The data are calculated assuming the standard luminosity of 10^{34} cm^{-2} s^{-1} running 10^7 s per year and a proton-proton cross section of 71 mb. The fluxes are plotted versus the radius of the inner detector. The dependence of fluxes on the z-direction (along the beam pipe) is less pronounced, towards higher values of z the fluxes increase roughly by a factor of two.

It can be seen in fig. 2.11 that for radii below 35 cm the particle flux is dominated by pions. Hence a comprehensive investigation on pion damage has been undertaken in the last two years (see e.g. [30, 31]). At radii greater than 35 cm the neutrons are the dominant particles. The other particles, protons, anti-protons, and kaons contribute only to a minor degree. Note that even at the outer barrel (R = 60 cm) the total equivalent fluence per year is greater than $5{\cdot}10^{12}$ cm^{-2}. Very close to the interaction point the annual fluence is about $6{\cdot}10^{13}$ cm^{-2} per year.

Chapter 3

Radiation Induced Bulk Defects

Radiation damage in silicon is generally divided into two categories; namely damage to the bulk and surface damage. Subject of investigation throughout this work is the bulk damage.

Radiation destroys locally the periodic structure of the lattice. Some of these dislocations establish energy levels in the band gap leading to a change of the electrical properties of silicon, and hence also of the detector. In the following firstly the mechanism of the defect generation and secondly the annealing of defects are considered. In the third section some specific identified defects which are of concern in radiation damage shall be reviewed. Finally it is described how defect levels affect the electrical properties of silicon detectors.

3.1 Defect Generation

The principal cause of bulk damage is the interaction of incoming particles and the lattice atoms either by collision triggering a displacement or by a nuclear reaction. Reactions relevant for direct defect generation are those that result in a nucleus of a different atomic number, because the product of the reaction is an impurity atom, which may influence the electrical properties of the silicon. Worth mentioning are the reactions which result in aluminium and magnesium : ^{28}Si(n,d)^{28}Al, ^{28}Si(n,d)^{27}Al and ^{28}Si(n,α)^{25}Mg. Aluminium is an acceptor, but the concentration produced is irrelevant, because ^{28}Al decays with a half-life period of 2.3 h and the cross section of the reaction producing ^{27}Al is too small. Magnesium is a donor and the generated concentration per fluence is about $g_{Mg} = 0.01$ cm^{-1} [32], and therefore considerable concentrations can be achieved by high fluence irradiation. However, the damage by nuclear reactions is dominated by the energy release of excited nuclei e.g. by emission of a gamma or an electron.

A lattice atom displaced by an incoming particle is termed *primary knock-on atom* (PKA) which may then take up an interstitial position in the lattice. The former site of the dislodged atom is known as a vacancy. A pair of a vacancy and an interstitial atom is called a *Frenkel defect* or a *close pair*. An average energy E_d of about 25 eV [33] is required to dislocate the PKA, if even more energy is transferred the PKA will lose the surplus of energy by ionisation or by causing further displacements which may proceed in a cascade manner. The maximum energy which can be transferred from a neutron of energy E_n to a silicon atom can

be deduced from kinematics of collision

$$E_{max,tr} = 4E_n \frac{m_n m_{Si}}{(m_n + m_{Si})^2}. \tag{3.1}$$

In the case of $E_n = 1$ MeV it is $E_{max,tr} \approx 130$ keV. As opposed to charged particles, which prefer transfer of only small energies, for neutrons all energy transfers in the entire range between E_d and $E_{max,tr}$ are of similar probability [34]. Because the cross section for elastic scattering of Si-Si interaction increases with lower energy, slowed-down atoms are likely to release the remaining kinetic energy in a very short range causing so-called *disordered regions* [35]. At least 5 keV are necessary to form a disordered region [33], which are also known as *clusters*.

Usually the damage caused by radiation is measured as function of dose, which is defined as absorbed energy per unit mass (1 Gy = 1 J / 1 kg). But the total energy release of a particle in a semiconductor is not an adequate measure, because the energy loss due to ionisation is a reversible process and causes no durable damage.[1] The damage in silicon corresponds to the *non-ionising energy loss* (NIEL) [36, 37]. The NIEL in turn scales linearly with the *displacement damage cross-section*, which is also called *damage function* $D(E_n)$. The NIEL has units of [keV cm^2 g^{-1}] and the displacement damage cross-section has units of [MeV mb]. For silicon it is

$$100 \text{ MeV mb} = 2.14 \text{ keV cm}^2 \text{ g}^{-1}.$$

The damage function is the adequate measure of the damage caused by a neutron, because it takes into account all possible reactions between neutrons and silicon atoms and also the fraction of energy the PKA releases in displacement collisions. In fig. 3.1 the damage function, or the NIEL is plotted versus the neutron energy. Because the damage function varies with the neutron energy it is not appropriate to compare directly the damage caused by neutrons of different energies. In order to allow a universal comparison of results it is common practice to refer to the equivalent fluence Φ_{eq} of 1 MeV neutrons which would have caused the same damage as the fluence Φ_{E_n} really applied. Φ_{E_n} converts to Φ_{eq} by just multiplying with the *hardness factor* κ :

$$\Phi_{eq} = \kappa \Phi_{E_n}. \tag{3.2}$$

In case of mono-energetic neutrons κ is simply the ratio $D(E_n)/D(1MeV)$, but in case of a spectral distribution $d\Phi/dE$ the full expression to calculate κ looks more complex :

$$\kappa = \frac{1}{D(1MeV)} \cdot \frac{\int D(E_n) \frac{d\Phi}{dE}(E_n)\, dE_n}{\int \frac{d\Phi}{dE}(E_n)\, dE_n}. \tag{3.3}$$

The standard value of the damage cross section at $E_n = 1$ MeV is $D(1 \text{ MeV}) = 95$ MeV mb [40]. In the energy range up to $E_n = 15$ MeV the damage function after Lazo [38] has been used, and above this range the data after van Ginneken [39], which are given in a wider step size. The values of κ applied to the fluences of the used neutron sources are given in tab. 5.2. Note, that in the following all given fluences Φ are equivalent to 1 MeV-neutrons. The index eq is omitted.

[1] The generated electron-hole pairs in silicon recombine, while e.g. in silicon oxide a recombination is rather unlikely.

Two classes of defects have to be considered now: clusters and Frenkel-defects. The generation rates (concentration per unit fluence Φ) of clusters and Frenkel-defects have been estimated by Wunstorf [36] :

$$g_{cluster} = 0.33 \text{ cm}^{-1},$$
$$g_{Frenkel} = 2.09 \text{ cm}^{-1},$$

where $g_{Frenkel}$ excludes the part of pairs, which recombine immediately.

Both constituents of the Frenkel-defect, the interstitial atom and the vacancy are highly mobile for temperatures above 4K, respectively 150K [41]. Migrating through the crystal they will form defect complexes, either with impurity atoms or with themselves. Typical reactions are listed in tab. 3.1. The most relevant defect configurations are shown schematically in fig. 3.2.

There are three dominant vacancy-related defects, namely the vacancy-oxygen pair V-O (A-centre [2]), the vacancy-phosphorus pair V-P (E-centre) and the divacancy V-V, which are stable at room temperature. The vacancy is also captured by other impurity atoms, but these formations are not stable. Applying dose rate dependent electron irradiation experiments, it has been found that divacancies are mainly produced by pairing of single vacancies generated within the same collision cascade. The pairing of vacancies generated in distances greater than about 50 nm is insignificant [42]. It is reasonable to assume the same behaviour also for neutron damage.

The interstitial atoms contribute to the complex formation mainly by replacing other atoms and recombining with vacancy related defects. Self displacement is

[2]The alphanumerical labelling of some defect-complexes originates from early electron paramagnetic resonance studies (EPR).

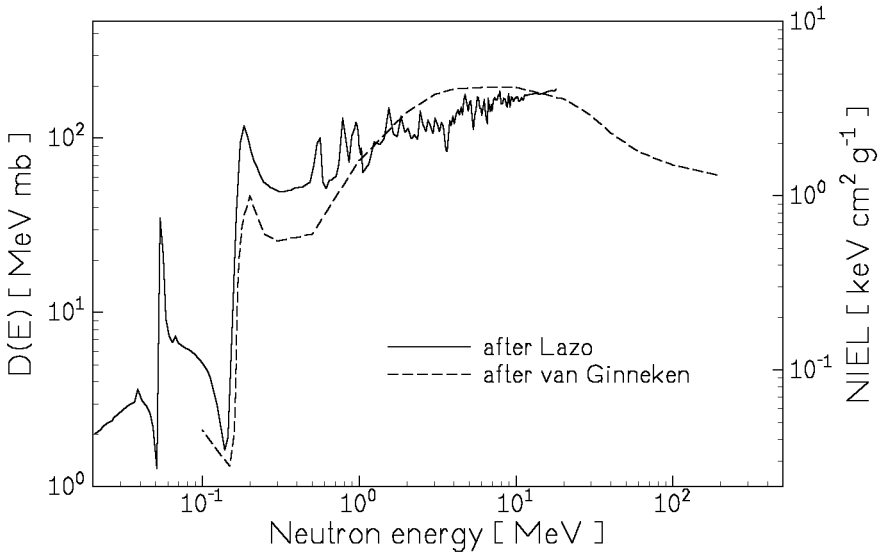

Figure 3.1: The calculated damage function and the non-ionising energy loss (NIEL) after Lazo [38] and van Ginneken [39] versus neutron energy. The range below 10^{-2} MeV is not relevant for the neutron fields used throughout this work (see sec. 5.2), but may be important in the case of spallation sources.